A discrete Funk transform on the Cubed Sphere

Jean-Baptiste Bellet

A DISCRETE FUNK TRANSFORM ON THE CUBED SPHERE

JEAN-BAPTISTE BELLET

Abstract. Computing accurately Funk transforms from discrete values is crucial in some applications, such as Q-Ball Imaging in medicine. This paper deals with a discrete Funk transform devoted to such a computation. The studied transform is based on a spectral method applied on a least squares fitting, with the special feature that regularization is not performed. We investigate several mathematical and numerical aspects in this context, including stability and pseudoinversion. As a specific instance, we introduce a simple framework based on the equiangular Cubed Sphere to guarantee the stability. Various numerical experiments attest to the accuracy and the convergence of the approach, in particular for synthetic Gaussian signals from Q-Ball Imaging.

1. Introduction

The Funk transform from [13], also called the Funk-Minkowski transform, the Funk-Radon transform, or the spherical Radon transform, is an integral transform which averages a function along great circles on the unit sphere $\mathbb{S}^2$. This transform, similar integral transforms, and associated inverse problems, are the subject of many mathematical studies, such as [19,25,29,34,37] and the references therein. These transforms play an important role in various applications, including photoacoustic tomography [20,44], Synthetic Aperture Radar [43] and diffusion Magnetic Resonance Imaging (dMRI) [22,41].

To specify one successful example from medicine, *Q-Ball Imaging* images the orientation of fibers in biological tissues [41]. The key step of this method computes the Funk transform of dMRI signals recorded on discrete spherical grids. The original computation [41] is a trapezoidal quadrature rule, applied on an interpolating function. The numerical scheme has been improved in [12,17], using a spectral method on a regularized least squares approximation. The success[1] of the articles [12, 17, 41] attests that it is crucial to master the Funk transform in discrete configurations.

So, this paper is devoted to a mathematical study of a discrete Funk transform, in order to provide new theoretical and numerical guarantees. The studied transform is a particular case of the approaches introduced in [12,17]; it is based on a spectral method combined with a least squares fitting. The main feature of this work is that we restrict our attention to least squares fitting without any regularization, so as to get a mathematical framework which is as clear as possible. The least squares functional comprises a fitting term, but it does not contain any artificial penalty. In particular, no regularization functional nor regularization weight have to be tuned in our approach.

The least squares problem fits values given on a spherical grid by a spherical harmonics with prescribed degree. The grid and the degree must be carefully chosen to insure that the problem is well-conditioned, which means that the corresponding matrix must have full column rank and a suitable condition number. This matrix, called a Vandermonde matrix as in [6, 26, 27], or an alternant matrix as in [1, p. 112], contains spherical harmonics restricted to the grid. In general, finding theoretically the rank and the condition number of such a matrix enters into the framework of harmonic analysis and is not an easy task. Geometrical and metric properties of the grid, as defined in [16,18], come into play. For example, [26, Theorem 2.4]– [27, Lemma 3.13]

Date: February 2, 2023.

2020 *Mathematics Subject Classification.* 65R10, 44A12, 92C55.

Key words and phrases. Cubed Sphere, least squares, spherical harmonics, Funk transform, Radon transform.

[1]The website of the journal *Magnetic Resonance in Medicine* mentions 1430 citations for [41], 283 citations for [17], and 559 citations for [12], on January 05, 2023.

give a lower bound on the degree to insure a full row rank property; this bound is inversely proportional to the separation distance. Another example is [2, Theorem 3.5], which proves a full column rank property, assuming that the mesh norm is smaller than the inverse of the degree.

Choosing or defining a spherical grid with suitable properties is itself an important subject. We refer to [42] for a historical presentation of several grids, and to [16] for a comparison of many popular grids, such as spiral grids, polyhedral grids, random grids, and so on. Some approaches compute an "optimal" grid as the numerical solution to an optimization problem; see for instance [9] for various optimization criteria, including the conditioning of a least squares problem. Some other approaches define grids in an elementary explicit way. Among these simple grids, the equiangular Cubed Sphere [36,38] is obtained by radial projection of a circumscribed cube, from cartesian lines on the faces of the cube towards great circles on the sphere.

This Cubed Sphere (and some variants) is very popular and is widely studied in numerical climatology and meteorology; see for instance [10,21,23,24,28,30–33,35,39]. We have recently studied various approximation schemes on this grid using spherical harmonics. Lagrange interpolation has been considered in [6], a spherical quadrature rule in [5], and least squares approximation in [7]. Among the results, [7] gives the largest degree which numerically guarantees a condition number that is uniformly bounded. In this paper, we propose a further study concerning spectral computing on the Cubed Sphere. We investigate for the first time the use of this grid for computing Funk transforms.

Our methodology contains two steps. In a first step, we define a family of discrete Funk transforms which act between spaces of grid functions, for a general grid. They are obtained as in [12,17], but without any regularization, and with an evaluation of the (continuous) transform on the initial grid. We prove new properties satisfied by these transforms, in order to give some mathematical background. In particular, we show that the pseudoinverse of such a transform represents an inverse discrete Funk transform very analogous to the direct one. We also provide a theoretical estimation of stability, which mainly depends on the conditioning of the least squares problem. It implies that stability is guaranteed as soon as the least squares problem is well-conditioned.

Therefore, in a second step, we focus on a framework which guarantees this condition of stability. We select the equiangular Cubed Sphere for the grid and we introduce a rule on the degree such that the conditioning is kept under control. The study is similar with [7], but the dimensions of the least squares problem have been reduced due to our specific problem. Indeed, the null space of the Funk transform contains any odd function, so we assume from the beginning that the approximation space contains only even spherical harmonics. Also, symmetry consideration allows to halve the grid, so we restrict the Cubed Sphere to an hemisphere.

The paper is organized as follows. In Section 2, we summarize some notation and background concerning spherical computation. In Section 3, we study a discrete Funk transform, based on a spectral method applied on a least squares fitting. In Section 4, we focus on the case where the grid is the equiangular Cubed Sphere. In Section 5, the relevance of the approach is shown by various numerical tests, such as test of accuracy and stability on synthetic dMRI signals.

2. Background and notation

2.1. **Spherical harmonics.** On the unit sphere $\mathbb{S}^2 = \{(x_1, x_2, x_3) \in \mathbb{R}^3 : x_1^2 + x_2^2 + x_3^2 = 1\}$, the spherical coordinates are given by

$$x(\theta, \phi) = (\cos\theta\cos\phi, \cos\theta\sin\phi, \sin\theta) \in \mathbb{S}^2, \quad \theta \in [-\tfrac{\pi}{2}, \tfrac{\pi}{2}],\ \phi \in \mathbb{R}.$$

In these coordinates, the real Legendre spherical harmonics of degree $n \geq 0$ are defined by

$$Y_n^m(x(\theta,\phi)) = \sqrt{\tfrac{(n+1/2)(n-|m|)!}{\pi(n+|m|)!}} P_n^{(|m|)}(\sin\theta) \cdot \cos^{|m|}\theta \cdot \begin{cases} -\sin m\phi, & -n \leq m < 0, \\ \frac{1}{\sqrt{2}}, & m = 0, \\ \cos m\phi, & 0 < m \leq n, \end{cases}$$

where $P_n^{(|m|)}(t) = \frac{\mathrm{d}^{|m|}}{\mathrm{d}t^{|m|}} P_n(t)$ is the $|m|$-th derivative of the Legendre polynomial of degree n, defined by

$$P_n(t) = \tfrac{1}{2^n n!} \tfrac{\mathrm{d}^n}{\mathrm{d}t^n}(t^2-1)^n.$$

The infinite family $(Y_n^m)_{|m|\leq n,\, n\in\mathbb{N}}$ is a Hilbert basis of the space $L^2(\mathbb{S}^2)$, which is equipped with the usual inner product and the associated norm,

$$\langle f, g\rangle_{L^2(\mathbb{S}^2)} = \int_{\mathbb{S}^2} f(x)g(x)\mathrm{d}\sigma, \quad \|f\|_{L^2(\mathbb{S}^2)} = \langle f, f\rangle_{L^2(\mathbb{S}^2)}^{1/2}.$$

In this basis, any $f \in L^2(\mathbb{S}^2)$ admits a unique spectral expansion,

$$f = \sum_{|m|\leq n} \hat{f}_n^m Y_n^m, \quad \text{with} \quad \hat{f}_n^m = \langle f, Y_n^m\rangle_{L^2(\mathbb{S}^2)}. \tag{1}$$

For a fixed degree $D \geq 0$, the subspace of the spherical harmonics with degree less than or equal to D is denoted by $\mathcal{Y}_D$, so that $(Y_n^m)_{|m|\leq n\leq D}$ is an orthonormal basis of $\mathcal{Y}_D$. The subspace of even functions in $\mathcal{Y}_D$, denoted by $\mathcal{Y}_D^{\mathrm{ev}}$, is spanned by the even degrees, *i.e.*

$$\mathcal{Y}_D^{\mathrm{ev}} = \mathrm{span}\{Y_{2n}^m,\, 0 \leq n \leq \tfrac{D}{2},\, |m| \leq 2n\}.$$

In the sequel, we always assume that the degree D is even when considering $\mathcal{Y}_D^{\mathrm{ev}}$ (because $\mathcal{Y}_D^{\mathrm{ev}} = \mathcal{Y}_{D-1}^{\mathrm{ev}}$ otherwise); under this assumption, the dimension of $\mathcal{Y}_D^{\mathrm{ev}}$ is given by

$$d_D = \tfrac{1}{2}(D+1)(D+2).$$

2.2. **Funk transform.** The Funk transform, denoted by $\mathcal{F}$, maps a spherical function $f : \mathbb{S}^2 \to \mathbb{R}$ to a spherical function $\mathcal{F}f : \mathbb{S}^2 \to \mathbb{R}$ as follows. For any unit vector $\alpha \in \mathbb{S}^2$, $\mathcal{F}f(\alpha)$ is defined as the average of f along the great circle that is orthogonal to α, *i.e.*

$$\mathcal{F}f(\alpha) = \frac{1}{2\pi} \int_{\{x\in\mathbb{S}^2 : x\cdot\alpha = 0\}} f\,\mathrm{d}s, \quad \alpha \in \mathbb{S}^2, \quad f : \mathbb{S}^2 \to \mathbb{R}, \tag{2}$$

where s denotes the length measure on the circle $\{x \in \mathbb{S}^2 : x \cdot \alpha = 0\}$; in this definition, the function f is required to be integrable along any great circle (with respect to the length measure), so that the integrals are defined.

The Funk transform $\mathcal{F}f$ is an even function, *i.e.* $\mathcal{F}f(-\alpha) = \mathcal{F}f(\alpha)$, $\alpha \in \mathbb{S}^2$. If f is odd, *i.e.* $f(-x) = -f(x)$, $x \in \mathbb{S}^2$, then $\mathcal{F}f = 0$. In any case, $\mathcal{F}f = \mathcal{F}f^{\mathrm{ev}}$, where $f^{\mathrm{ev}}(x) = \frac{1}{2}(f(x)+f(-x))$ denotes the even part of f. For these reasons, the Funk transform can be considered between spaces of even functions, without loss of generality. We follow this convention throughout the article. Hence, in the sequel, we consider even functions only.

Spherical harmonics are eigenfunctions of the Funk transform $\mathcal{F}$ [13], so that it defines an isomorphism on $\mathcal{Y}_D^{\mathrm{ev}}$,

$$\mathcal{F} : \mathcal{Y}_D^{\mathrm{ev}} \to \mathcal{Y}_D^{\mathrm{ev}}, \quad \mathcal{F}Y_{2n}^m = P_{2n}(0)\, Y_{2n}^m, \quad \text{with} \quad P_{2n}(0) = (-1)^n \tfrac{1\cdot 3\cdot 5\cdots(2n-1)}{2\cdot 4\cdot 6\cdots(2n)}, \quad |m| \leq 2n,\, 0 \leq n \leq \tfrac{D}{2}. \tag{3}$$

The associated nonsingular matrix is the block diagonal matrix

$$\Lambda = \mathrm{diag}\left[(-1)^n \tfrac{1\cdot 3\cdot 5\cdots(2n-1)}{2\cdot 4\cdot 6\cdots(2n)} \mathrm{I}_{4n+1}, 0 \leq n \leq \tfrac{D}{2}\right] \in \mathbb{R}^{d_D \times d_D}. \tag{4}$$

This structure suggests the spectral method for computing Funk transforms, as it has been introduced in [12, 17].

2.3. **Grid functions.** A spherical grid is a finite subset of the unit sphere, $G \subset \mathbb{S}^2$. A grid function on G is a function $b : G \to \mathbb{R}$ defined on G. The space of such functions is denoted by

$$\mathbb{R}^G = \{b : G \to \mathbb{R}\}.$$

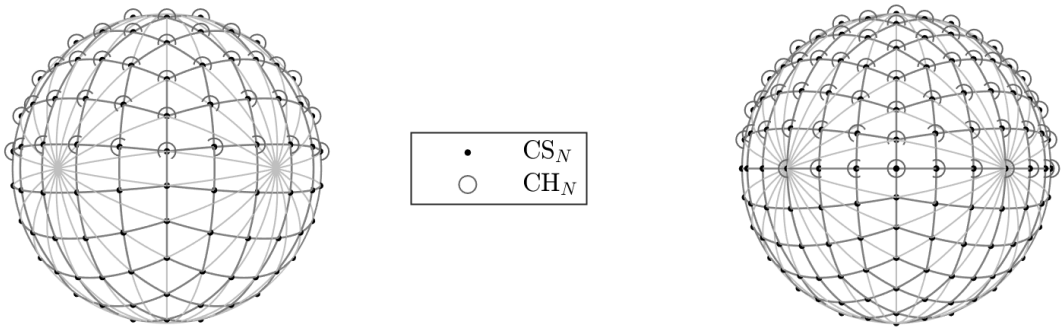

FIGURE 1. Cubed Sphere and Cubed Hemisphere. The Cubed Sphere CS_N (black dots) defined in (5) is obtained by intersecting equiangular meridian circles (gray lines). The Cubed Hemisphere CH_N (gray circles) defined in (19) is located in the Northern hemisphere; it contains half of the points from CS_N. Left: N is odd ($N = 5$). Right: N is even ($N = 6$).

Numbering the elements of G by $\xi_1, \dots, \xi_M$, where M denotes the cardinal number, the canonical basis $(\delta_{\xi_i})_{1 \leq i \leq M}$ of $\mathbb{R}^G$ is defined by

$$\delta_{\xi_i}(\xi_j) = \begin{cases} 1, \text{ if } i = j, \\ 0, \text{ otherwise,} \end{cases} \qquad 1 \leq i, j \leq M.$$

In this basis, any $b \in \mathbb{R}^G$ is represented by the column vector $\boldsymbol{b} = [b(\xi_i)]_{1 \leq i \leq M} \in \mathbb{R}^M$, due to

$$b = \sum_{i=1}^{M} b(\xi_i) \delta_{\xi_i}.$$

For any real function defined on the sphere, $f : \mathbb{S}^2 \to \mathbb{R}$, the restriction of f on the grid G is the grid function $f|_G \in \mathbb{R}^G$ defined by

$$f|_G := \sum_{i=1}^{M} f(\xi_i) \delta_{\xi_i}, \quad f|_G(\xi_i) = f(\xi_i),\ 1 \leq i \leq M.$$

2.4. **Cubed Sphere.** For a fixed parameter $N \geq 1$, the equiangular Cubed Sphere $\mathrm{CS}_N \subset \mathbb{S}^2$ with angular step $\frac{\pi}{2N}$, is depicted in Figure 1; it is defined analytically by

$$\mathrm{CS}_N := \left\{ \xi \in \mathbb{S}^2 : \exists (i,j,k) \in \mathbb{N}^3 \cap \partial([0,N]^3), \quad \xi = \Psi(-\tfrac{\pi}{4} + \tfrac{i\pi}{2N}, -\tfrac{\pi}{4} + \tfrac{j\pi}{2N}, -\tfrac{\pi}{4} + \tfrac{k\pi}{2N}) \right\}, \qquad (5)$$
$$\text{with } \Psi(\alpha,\beta,\gamma) := \tfrac{(\tan\alpha, \tan\beta, \tan\gamma)}{(\tan^2\alpha + \tan^2\beta + \tan^2\gamma)^{1/2}},\ (\alpha,\beta,\gamma) \in \partial([-\tfrac{\pi}{4}, \tfrac{\pi}{4}]^3).$$

In this definition, CS_N is browsed as follows. The triplet (α, β, γ) browses a uniform grid of angles, on the faces of the cube $[-\frac{\pi}{4}, \frac{\pi}{4}]^3$; the angular step is $\frac{\pi}{2N}$. This triplet is mapped to the point $(\tan\alpha, \tan\beta, \tan\gamma)$, which browses a cartesian grid on the faces of the cube $[-1, 1]^3$. Lastly, the radial projection of this point to the sphere is $\xi = \Psi(\alpha, \beta, \gamma)$, which browses CS_N. From a geometrical point of view, CS_N can be obtained by intersecting great circles as in Figure 1. These great circles correspond to $2N$ equiangular meridian circles with polar axis $(0; (0,0,1))$, and their counterparts for the axes $(0; (0,1,0))$ and $(0; (1,0,0))$. The cardinal number of CS_N is given by $6N^2 + 2$ (see, for instance, [8]).

3. Discrete Funk transform on a spherical grid

In this section, we study a discrete Funk transform on a general grid. We assume that

- $G = \{\xi_1, \dots, \xi_M\} \subset \mathbb{S}^2$ is a spherical grid with cardinal number M,
- $b \in \mathbb{R}^G$ is a given grid function on G,
- $D \geq 0$ is a fixed even degree.

3.1. **Least squares fitting.** One looks for an even spherical harmonics $f \in \mathcal{Y}_D^{\mathrm{ev}}$ which fits the grid function b. The least squares problem minimizes a fitting error as follows,

$$\inf_{f \in \mathcal{Y}_D^{\mathrm{ev}}} \sum_{i=1}^{M} (f(\xi_i) - b(\xi_i))^2. \tag{LS}$$

We introduce the basis (Y_{2n}^m) of $\mathcal{Y}_D^{\mathrm{ev}}$. Then any $f \in \mathcal{Y}_D^{\mathrm{ev}}$ admits a spectral expansion (1),

$$f = \sum_{0 \le n \le D/2,\, |m| \le 2n} \hat{f}_{2n}^m Y_{2n}^m \in \mathcal{Y}_D^{\mathrm{ev}}, \quad \text{with} \quad \hat{f} = [\hat{f}_{2n}^m]_{0 \le n \le D/2,\, |m| \le 2n} \in \mathbb{R}^{d_D};$$

the matrix of the linear map $f \in \mathcal{Y}_D^{\mathrm{ev}} \mapsto [f(\xi_i)]_{1 \le i \le M} \in \mathbb{R}^M$ is given by the Vandermonde matrix

$$A = [Y_{2n}^m(\xi_i)]_{\substack{1 \le i \le M \\ 0 \le n \le D/2,\, |m| \le 2n}} \in \mathbb{R}^{M \times d_D}. \tag{6}$$

Here, the row index is i, and the column index is the couple (n, m). Assuming a lexicographic ordering for (n, m), an expanded form of A is given by

$$A = \begin{bmatrix} Y_0^0(\xi_1) & \cdots & Y_{2n}^{-2n}(\xi_1) & \cdots & Y_{2n}^m(\xi_1) & \cdots & Y_{2n}^{2n}(\xi_1) & \cdots & Y_D^D(\xi_1) \\ \vdots & & \vdots & & \vdots & & \vdots & & \vdots \\ Y_0^0(\xi_i) & \cdots & Y_{2n}^{-2n}(\xi_i) & \cdots & Y_{2n}^m(\xi_i) & \cdots & Y_{2n}^{2n}(\xi_i) & \cdots & Y_D^D(\xi_i) \\ \vdots & & \vdots & & \vdots & & \vdots & & \vdots \\ Y_0^0(\xi_M) & \cdots & Y_{2n}^{-2n}(\xi_M) & \cdots & Y_{2n}^m(\xi_M) & \cdots & Y_{2n}^{2n}(\xi_M) & \cdots & Y_D^D(\xi_M) \end{bmatrix}.$$

Then, the problem (LS) can be written in matrix form as

$$\inf_{\hat{f} \in \mathbb{R}^{d_D}} \|A\hat{f} - \boldsymbol{b}\|^2,$$

where $\|\cdot\|$ denotes the euclidean norm in $\mathbb{R}^M$.

In this paper, we assume that the grid G and the degree D are such that the Vandermonde matrix A has full column rank. Then the problem (LS) admits a unique solution. This solution, denoted[2] by

$$\ell[b] \in \mathcal{Y}_D^{\mathrm{ev}}, \quad \ell[b] = \arg\inf_{f \in \mathcal{Y}_D^{\mathrm{ev}}} \sum_{i=1}^{M} (f(\xi_i) - b(\xi_i))^2, \tag{7}$$

is given by

$$\ell[b] = [Y_{2n}^m(\cdot)]_{0 \le n \le D/2,\, |m| \le 2n}^{\intercal}\, \widehat{\ell[b]}, \quad \text{with} \quad \widehat{\ell[b]} = (A^{\intercal}A)^{-1}A^{\intercal}\boldsymbol{b} \in \mathbb{R}^{d_D}. \tag{8}$$

Here, the vector $\widehat{\ell[b]}$ of the spectral coefficients satisfies a linear system, whose matrix is symmetric and positive-definite:

$$A^{\intercal}A\, \widehat{\ell[b]} = A^{\intercal}\boldsymbol{b}.$$

For the matrix norm induced by the euclidean norm, the condition number of this linear system is given by

$$\mathrm{cond}(A^{\intercal}A) = \mathrm{cond}(A)^2, \quad \text{with} \quad \mathrm{cond}(A) = \frac{\sigma_{\max}(A)}{\sigma_{\min}(A)},$$

where $\sigma_{\max}$, resp. $\sigma_{\min}$, denote the maximum, resp. minimum, singular value. In Section 4, we propose a choice of G and D which guarantees (at least numerically) that the condition number of the Vandermonde matrix is close to 1 ($\mathrm{cond}\, A \approx 1$).

Remark 1. If the condition number is large ($\mathrm{cond}\, A \gg 1$), or if A has not full column rank, then regularization is needed. This is outside the scope of this paper, so we refer in this case to [15] for a general reference about ill-posed problems, [3] for various regularization operators dealing with spherical harmonics on the sphere, and [12, 17] for regularization in a framework of Funk transforms.

[2] ℓ as the first letter of "least squares".

We conclude this subsection by a simple result which permits to halve the grid in the case of a central symmetry, provided that the grid function is replaced by its even part.

Proposition 2. *Assume that G in invariant with respect to the central symmetry, so that M is even, and $\xi_{M/2+i} = -\xi_i$, $1 \leq i \leq M/2$ (up to a reordering). Then the problem* (LS) *is equivalent to*

$$\inf_{f \in \mathcal{Y}_D^{\mathrm{ev}}} \sum_{i=1}^{M/2} (f(\xi_i) - b^{\mathrm{ev}}(\xi_i))^2, \quad \textit{with} \quad b^{\mathrm{ev}}(\xi_i) = \tfrac{1}{2}(b(\xi_i) + b(-\xi_i)),\ 1 \leq i \leq M/2.$$

Proof. The grid is invariant under the central symmetry $-\mathrm{I}_3$ ($\xi \leftrightarrow -\xi$), so we split the grid function b into $b = b^{\mathrm{ev}} + b^{\mathrm{odd}}$, where $b^{\mathrm{ev}}(\xi) = \frac{1}{2}(b(\xi) + b(-\xi))$ is an even grid function ($b^{\mathrm{ev}}(-\xi) = b^{\mathrm{ev}}(\xi)$), and $b^{\mathrm{odd}}(\xi) = \frac{1}{2}(b(\xi) - b(-\xi))$ is odd ($b^{\mathrm{odd}}(-\xi) = -b^{\mathrm{odd}}(\xi)$). Therefore, for any $f \in \mathcal{Y}_D^{\mathrm{ev}}$,

$$\sum_{i=1}^{M} (f(\xi_i) - b(\xi_i))^2 = \sum_{i=1}^{M} (f(\xi_i) - b^{\mathrm{ev}}(\xi_i))^2 + \sum_{i=1}^{M} b^{\mathrm{odd}}(\xi_i)^2 - 2\sum_{i=1}^{M} (f(\xi_i) - b^{\mathrm{ev}}(\xi_i)) b^{\mathrm{odd}}(\xi_i).$$

In the right hand side, the first term is twice the sum indexed by $1 \leq i \leq M/2$, because $(f - b^{\mathrm{ev}})^2$ is an even grid function. The second term is a constant C which does not depend on f. The third term is null, because $(f - b^{\mathrm{ev}})b^{\mathrm{odd}}$ is an odd grid function. Therefore,

$$\sum_{i=1}^{M} (f(\xi_i) - b(\xi_i))^2 = 2\sum_{i=1}^{M/2} (f(\xi_i) - b^{\mathrm{ev}}(\xi_i))^2 + C,$$

which proves the result. □

3.2. **Discrete Funk transform.** We study various mathematical properties of a discrete Funk transform defined as follows.

Definition 3 (Discrete Funk transform)**.** Let $G = \{\xi_1, \ldots, \xi_M\} \subset \mathbb{S}^2$ be a spherical grid and $D \geq 0$ be an even degree, such that the Vandermonde matrix A in (6) has full column rank. The discrete Funk transform F is defined as a linear mapping between spaces of grid functions, by

$$\begin{array}{rccc} \mathrm{F}: & \mathbb{R}^G & \longrightarrow & \mathbb{R}^G \\ & b & \longmapsto & \mathrm{F}[b] = \left(\mathcal{F}(\ell[b])\right)\Big|_G, \end{array} \tag{9}$$

where $\ell[b]$ is the least squares fitting in (7), and $\mathcal{F}$ is the Funk transform in (2). In other words, the discrete Funk transform of a grid function is the Funk transform applied on the least squares fitting, then restricted to the initial grid.

Property 4. *In the basis $(\delta_{\xi_i})_{1 \leq i \leq M}$ of $\mathbb{R}^G$, the matrix of the discrete Funk transform* F *is given by*

$$\mathbf{F} = A\,\Lambda\,(A^\intercal A)^{-1} A^\intercal \in \mathbb{R}^{M \times M}. \tag{10}$$

Proof. The matrix of the least squares operator, $\ell : \mathbb{R}^G \to \mathcal{Y}_D^{\mathrm{ev}}$, in the bases (δ_{ξ_i}) and (Y_{2n}^m), is given by $(A^\intercal A)^{-1} A^\intercal$, due to (8). The matrix of the Funk transform $\mathcal{F} : \mathcal{Y}_D^{\mathrm{ev}} \to \mathcal{Y}_D^{\mathrm{ev}}$, in the basis (Y_{2n}^m), is the matrix Λ in (4). And the matrix of $f \in \mathcal{Y}_D^{\mathrm{ev}} \mapsto f|_G \in \mathbb{R}^G$, in the bases (Y_{2n}^m) and (δ_{ξ_i}), is given by the Vandermonde matrix A. The discrete Funk transform F is the composition of these linear maps, so its matrix $\mathbf{F}$ is given by the product of the matrices. □

The following result establishes that the spherical function $\mathcal{F}(\ell[b])$ can be exactly recovered from its restriction $\mathrm{F}b$ on G (so that the restriction is here "lossly").

Proposition 5. *The discrete Funk transform $\mathrm{F} : \mathbb{R}^G \to \mathbb{R}^G$ and the Funk transform $\mathcal{F} : \mathcal{Y}_D^{\mathrm{ev}} \to \mathcal{Y}_D^{\mathrm{ev}}$ are related by*

$$\ell \circ \mathrm{F} = \mathcal{F} \circ \ell.$$

In other words, the least squares fitting of the discrete Funk transform coincides with the Funk transform of the least squares fitting,

$$\ell[\mathrm{F}b](\alpha) = \mathcal{F}(\ell[b])(\alpha), \quad b \in \mathbb{R}^G,\ \alpha \in \mathbb{S}^2.$$

Proof. Similarly as the proof of Property 4, the matrix of $\ell \circ \mathrm{F}$ is given by

$$(A^\intercal A)^{-1} A^\intercal \cdot A \Lambda \, (A^\intercal A)^{-1} A^\intercal = \Lambda \, (A^\intercal A)^{-1} A^\intercal,$$

where we recognize the matrix of $\mathcal{F} \circ \ell$ on the right hand side. □

In practice, $f : \mathbb{S}^2 \to \mathbb{R}$ is a spherical function that is sampled on the grid G, so that the given data is $b = f|_G$. One uses the discrete Funk transform $\mathrm{F}[f|_G]$, or equivalently $\mathcal{F}(\ell[f|_G])$, in order to approximate some values $\mathcal{F}f(\alpha)$ of the Funk transform $\mathcal{F}f$. The following result shows that this method is exact if $f \in \mathcal{Y}_D^{\mathrm{ev}}$.

Theorem 6 (Exactness on $\mathcal{Y}_D^{\mathrm{ev}}$). *The discrete Funk transform is exact on $\mathcal{Y}_D^{\mathrm{ev}}$, which means that*

$$\mathrm{F}[f|_G] = (\mathcal{F}f)|_G, \quad f \in \mathcal{Y}_D^{\mathrm{ev}}. \tag{11}$$

More generally, for every $f \in \mathcal{Y}_D^{\mathrm{ev}}$, the Funk transform $\mathcal{F}f$ can be computed exactly from the grid function $f|_G$, with

$$\mathcal{F}f(\alpha) = [Y_{2n}^m(\alpha)]_{0 \le n \le D/2, |m| \le 2n}^\intercal \Lambda \, (A^\intercal A)^{-1} \, A^\intercal \, [f(\xi_i)]_{1 \le i \le M}, \quad \alpha \in \mathbb{S}^2, \quad f \in \mathcal{Y}_D^{\mathrm{ev}}. \tag{12}$$

Proof. Any function $f \in \mathcal{Y}_D^{\mathrm{ev}}$ fits exactly the grid values $[f(\xi_i)]_{1 \le i \le M}$, so that the unique solution of (LS) with $b = f|_G$ is the initial function f itself,

$$\ell[f|_G] = f, \quad f \in \mathcal{Y}_D^{\mathrm{ev}}.$$

Injecting this equality into the definition of $\mathrm{F}[f|_G]$ proves (11). Also, we obtain $\mathcal{F}f = \mathcal{F}(\ell[f|_G])$; hence, we have (12) due to the matrix of $\mathcal{F} \circ \ell$ (see the proof of Proposition 5). □

Now, we investigate the inversion of the discrete Funk transform F. We introduce the Moore-Penrose pseudoinverse $\mathbf{F}^\dagger$ of the matrix $\mathbf{F}$, since it is not expected to be nonsingular. We refer to [14, pp. 257-258] for usual consideration about such a pseudoinverse. In our case, the pseudoinverse $\mathbf{F}^\dagger$ maps any $\boldsymbol{c} \in \mathbb{R}^M$ to the minimum norm solution $\boldsymbol{b} = \mathbf{F}^\dagger \boldsymbol{c} \in \mathbb{R}^M$ of the least squares problem $\inf_{\boldsymbol{b} \in \mathbb{R}^M} \|\mathbf{F}\boldsymbol{b} - \boldsymbol{c}\|^2$. We prove that the pseudoinverse $\mathbf{F}^\dagger$ represents an *inverse discrete Funk transform* that is analogous to the direct transform F.

Theorem 7 (Pseudoinversion). *The Moore-Penrose pseudoinverse of $\mathbf{F}$ is given by*

$$\mathbf{F}^\dagger = A \, \Lambda^{-1} \, (A^\intercal A)^{-1} A^\intercal \in \mathbb{R}^{M \times M}. \tag{13}$$

Therefore, the pseudoinverse $\mathbf{F}^\dagger$ represents the inverse discrete Funk transform $\mathrm{F}^\dagger$*, defined by*

$$\begin{array}{rccl} \mathrm{F}^\dagger : & \mathbb{R}^G & \longrightarrow & \mathbb{R}^G \\ & c & \longmapsto & \mathrm{F}^\dagger[c] = \left(\mathcal{F}^{-1}(\ell[c]) \right) \Big|_G . \end{array} \tag{14}$$

Proof. The matrix $\mathbf{F}^\dagger$ is the Moore-Penrose pseudoinverse of $\mathbf{F}$ (and conversely), because (10) and (13) imply that the four Moore-Penrose conditions [14, p. 257] are satisfied:

$$\mathbf{F}\mathbf{F}^\dagger\mathbf{F} = \mathbf{F}, \quad \mathbf{F}^\dagger\mathbf{F}\mathbf{F}^\dagger = \mathbf{F}^\dagger, \quad (\mathbf{F}\mathbf{F}^\dagger)^\intercal = \mathbf{F}\mathbf{F}^\dagger, \quad (\mathbf{F}^\dagger\mathbf{F})^\intercal = \mathbf{F}^\dagger\mathbf{F}.$$

Furthermore, the matrix of the transform $\mathrm{F}^\dagger$ defined in (14) is given by $\mathbf{F}^\dagger$. This result and its proof are analogous to Property 4. The difference is that the diagonal matrix Λ of the isomorphic Funk transform $\mathcal{F} : \mathcal{Y}_D^{\mathrm{ev}} \to \mathcal{Y}_D^{\mathrm{ev}}$ is replaced by the inverse diagonal matrix Λ^{-1}, since it represents the inverse transform $\mathcal{F}^{-1}$. □

The relations (9) and (14) are very similar, so are (10) and (13). More generally, as soon as some result is established for one of the transforms F and $\mathrm{F}^\dagger$, some counterpart is expected for the other one. For instance, the counterpart of Proposition 5 is given hereafter.

Proposition 8. *The inverse discrete Funk transform $\mathrm{F}^\dagger : \mathbb{R}^G \to \mathbb{R}^G$ and the inverse Funk transform $\mathcal{F}^{-1} : \mathcal{Y}_D^{\mathrm{ev}} \to \mathcal{Y}_D^{\mathrm{ev}}$ satisfy*

$$\ell \circ \mathrm{F}^\dagger = \mathcal{F}^{-1} \circ \ell.$$

In other words, the least squares fitting of the inverse discrete Funk transform coincides with the inverse Funk transform of the least squares fitting,

$$\ell[\mathrm{F}^\dagger c](\xi) = \mathcal{F}^{-1}(\ell[c])(\xi), \quad c \in \mathbb{R}^G, \, \xi \in \mathbb{S}^2.$$

Proof. Analogous to the proof of Proposition 5. □

Now, we express mapping properties of $\mathbf{F}$ and $\mathbf{F}^\dagger$ in term of the Vandermonde matrix A.

Proposition 9. *The following assertions hold.*

(i) The composition of $\mathbf{F}$ *and* $\mathbf{F}^\dagger$ *coincides with the orthogonal projection on* $\operatorname{Ran} A$,

$$\mathbf{F}\mathbf{F}^\dagger = \mathbf{F}^\dagger\mathbf{F} = A(A^\intercal A)^{-1}A^\intercal. \tag{15}$$

In particular,

$$\forall \boldsymbol{b} \in \operatorname{Ran} A, \quad \mathbf{F}^\dagger\mathbf{F}\,\boldsymbol{b} = \mathbf{F}\mathbf{F}^\dagger\,\boldsymbol{b} = \boldsymbol{b}. \tag{16}$$

(ii) The null space and the range of $\mathbf{F}$ *satisfy*

$$\operatorname{Ker}\mathbf{F} = \operatorname{Ker} A^\intercal = (\operatorname{Ran} A)^\perp, \quad \operatorname{Ran}\mathbf{F} = \operatorname{Ran} A, \quad \mathbb{R}^M = \operatorname{Ker}\mathbf{F} \overset{\perp}{\oplus} \operatorname{Ran}\mathbf{F}.$$

(iii) The null space and the range of $\mathbf{F}^\dagger$ *satisfy* $\operatorname{Ker}\mathbf{F}^\dagger = \operatorname{Ker}\mathbf{F}$, $\operatorname{Ran}\mathbf{F}^\dagger = \operatorname{Ran}\mathbf{F}$.

Proof. (i) Since A has full column rank, the orthogonal projection on $\operatorname{Ran} A$ is given by the matrix $\Pi = A(A^\intercal A)^{-1}A^\intercal$. Then $\mathbf{F}\mathbf{F}^\dagger = \mathbf{F}^\dagger\mathbf{F} = \Pi$ can be easily checked with (10) and (13). And this implies (16) due to $\Pi\boldsymbol{b} = \boldsymbol{b}$, for any $\boldsymbol{b} \in \operatorname{Ran} A$.
(ii) The orthogonal decomposition $\mathbb{R}^M = \operatorname{Ker} A^\intercal \oplus \operatorname{Ran} A$ is a consequence of classical linear algebra. Secondly, $\operatorname{Ker} A^\intercal \subset \operatorname{Ker}\mathbf{F}$ is easily seen in (10), and $\operatorname{Ker}\mathbf{F} \subset \operatorname{Ker}\mathbf{F}^\dagger\mathbf{F} = \operatorname{Ker}\Pi$, with $\operatorname{Ker}\Pi = (\operatorname{Ran} A)^\perp = \operatorname{Ker} A^\intercal$. Thirdly, $\operatorname{Ran}\mathbf{F} \subset \operatorname{Ran} A$ is easily seen in (10); furthermore, (16) proves that $\operatorname{Ran} A \subset \operatorname{Ran}\mathbf{F}\mathbf{F}^\dagger$, with $\operatorname{Ran}\mathbf{F}\mathbf{F}^\dagger \subset \operatorname{Ran}\mathbf{F}$. The last equality is a consequence of the first two ones.
(iii) The null space and the range of $\mathbf{F}^\dagger$ are obtained analogously as those of $\mathbf{F}$. □

Translating this proposition to grid functions results in the following corollary.

Corollary 10. *The following asssertions hold.*

(i) The composition of F *and* $\mathrm{F}^\dagger$ *coincides with the restriction of the least squares fitting,*

$$\mathrm{F}\circ\mathrm{F}^\dagger = \mathrm{F}^\dagger\circ\mathrm{F}: \begin{array}{ccc} \mathbb{R}^G & \longrightarrow & \mathbb{R}^G \\ b & \longmapsto & \ell[b]|_G\,. \end{array} \tag{17}$$

(ii) The transform $\mathrm{F}^\dagger$ *is the usual inverse transform of* F*, if the spaces are restricted to the subspace* $\mathcal{Y}_D^{\mathrm{ev}}|_G := \{f|_G,\, f \in \mathcal{Y}_D^{\mathrm{ev}}\}$, i.e., *the linear mappings*

$$b \in \mathcal{Y}_D^{\mathrm{ev}}|_G \mapsto \mathrm{F}b \in \mathcal{Y}_D^{\mathrm{ev}}|_G, \quad c \in \mathcal{Y}_D^{\mathrm{ev}}|_G \mapsto \mathrm{F}^\dagger c \in \mathcal{Y}_D^{\mathrm{ev}}|_G,$$

are two isomorphisms which are inverses of each other.

Proof. (i) The relation (17) is the translation of (15), from matrices to their linear maps.
(ii) The subspace $\mathcal{Y}_D^{\mathrm{ev}}|_G \subset \mathbb{R}^G$ is the translation to grid functions of the space $\operatorname{Ran} A$. Translating (16) shows that

$$\forall b \in \mathcal{Y}_D^{\mathrm{ev}}|_G, \quad (\mathrm{F}\circ\mathrm{F}^\dagger)(b) = (\mathrm{F}^\dagger\circ\mathrm{F})(b) = b.$$

The combination of this result with Proposition 9.(ii-iii) shows the result. □

To finish with, we provide estimations of stability. They show that stability is expected if the condition number of the Vandermonde matrix A is suitable.

Theorem 11 (Stability)**.** *The maximum singular value of* $\mathbf{F}$*, resp.* $\mathbf{F}^\dagger$*, satisfies*

$$\sigma_{\max}(\mathbf{F}) \leq \operatorname{cond} A, \quad \sigma_{\max}(\mathbf{F}^\dagger) \leq \frac{\operatorname{cond} A}{|P_{2N-2}(0)|} \underset{N\to\infty}{\sim} \sqrt{\pi N}\operatorname{cond} A. \tag{18}$$

Remark 12. The largest singular values represent stability constants, since perturbing a vector $\boldsymbol{b} \in \mathbb{R}^M$ by $\boldsymbol{\epsilon} \in \mathbb{R}^M$ induces a perturbation on the transform $\mathbf{F}\boldsymbol{b}$, resp. $\mathbf{F}^\dagger\boldsymbol{b}$, which satisfies $\|\mathbf{F}(\boldsymbol{b}+\boldsymbol{\epsilon}) - \mathbf{F}\boldsymbol{b}\| \leq \sigma_{\max}(\mathbf{F})\|\boldsymbol{\epsilon}\|$, $\|\mathbf{F}^\dagger(\boldsymbol{b}+\boldsymbol{\epsilon}) - \mathbf{F}^\dagger\boldsymbol{b}\| \leq \sigma_{\max}(\mathbf{F}^\dagger)\|\boldsymbol{\epsilon}\|$.

Proof. The maximum singular value $\sigma_{\max}$ coincides with the matrix norm induced by the euclidean norm and is therefore sub-multiplicative. Hence, we deduce from (10) that

$$\sigma_{\max}(\mathbf{F}) \leq \sigma_{\max}(A)\,\sigma_{\max}(\Lambda)\,\sigma_{\max}(A^\dagger),$$

where $A^\dagger = (A^\intercal A)^{-1}A^\intercal$ is the Moore-Penrose pseudoinverse of the injective matrix A. On the right hand-side, $\sigma_{\max}(\Lambda) = P_0(0) = 1$, and $\sigma_{\max}(A^\dagger) = \frac{1}{\sigma_{\min}(A)}$ is the inverse of the minimum singular value of A. Therefore,

$$\sigma_{\max}(\mathbf{F}) \leq \frac{\sigma_{\max}(A)}{\sigma_{\min}(A)} = \operatorname{cond}(A).$$

For similar reasons, we see with (13) that

$$\sigma_{\max}(\mathrm{F}^\dagger) \leq \sigma_{\max}(A)\,\sigma_{\max}(\Lambda^{-1})\,\sigma_{\max}(A^\dagger) = \frac{\operatorname{cond}(A)}{|P_{2N-2}(0)|}.$$

Here, $\sigma_{\max}(\Lambda^{-1}) = \frac{1}{|P_{2N-2}(0)|}$, with $P_{2N-2}(0)$ given by (3); the asymptotics $\frac{1}{|P_{2N-2}(0)|} \sim \sqrt{\pi N}$ can checked with the Stirling formula $n! \sim \sqrt{2\pi n}\exp(-n)n^n$. □

4. Discrete Funk transform on the Cubed Hemisphere

In this section, we investigate the discrete Funk transform in the case of the equiangular Cubed Sphere CS_N.

4.1. **Cubed Hemisphere.** To begin with, for every $N \geq 1$, the grid CS_N is invariant under the central symmetry [4]. Hence, Proposition 2 shows that any least squares problem (LS) on this grid can be reduced to a problem on a half-grid, without changing the solution. Therefore, we restrict the grid CS_N to the Northern hemisphere and a half of the equator circle, without loss of generality. The resulting grid is displayed in Figure 1 and is defined below.

Definition 13. Let $N \geq 1$. The *Cubed Hemisphere* CH_N is defined by

$$\mathrm{CH}_N = \mathrm{CS}_N \cap \{x(\theta,\phi) \in \mathbb{S}^2, \quad (\theta > 0 \text{ and } 0 \leq \phi < 2\pi) \text{ or } (\theta = 0 \text{ and } 0 \leq \phi < \pi)\}, \tag{19}$$

so that CS_N splits into $\mathrm{CS}_N = \mathrm{CH}_N \cup (-\mathrm{CH}_N)$, and CH_N has the cardinal number $3N^2+1$.

In the remainder of this section, we consider the grid

$$G = \mathrm{CH}_N = \{\xi_i,\, 1 \leq i \leq M\}, \quad M = 3N^2+1,$$

where $N \geq 1$ is fixed.

4.2. **Degree.** We tune the degree D in term of the parameter N, so that the problem (LS) is well-conditioned. We argue that the value $D = 2N-2$ is a suitable choice.

The main motivation is the following claim.

Claim 14. *Let $N \geq 1$, $G = \mathrm{CH}_N$, and $D = 2N-2$. Then, the corresponding Vandermonde matrix $A \in \mathbb{R}^{(3N^2+1)\times(2N-1)N}$ defined in (6) has full column rank and is well-conditioned, with a condition number uniformly bounded with N.*

Unfortunately, a complete proof of Claim 14 is not available yet. The most convincing argument that we have at disposal is the numerical evidence displayed in Figure 2. These numerical results indicate that

$$\operatorname{cond} A \leq 2^{1/4} \leq 1.2, \quad 1 \leq N \leq 64,$$

and they suggest that $\operatorname{cond} A$ grows to $2^{1/4}$ when $N \to \infty$. We also have a partial proof, concerning the full column rank property in the case $N \leq 4$.

Theorem 15. *Assume that $1 \leq N \leq 4$, $G = \mathrm{CH}_N$, and consider the degree $D = 2N-2$. Then, the Vandermonde matrix A in (6) has full column rank.*

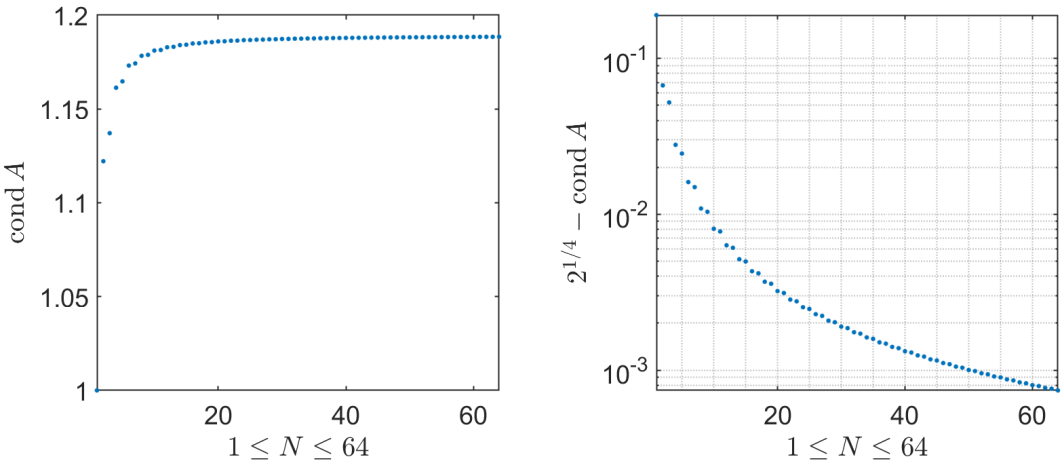

FIGURE 2. Numerical evidence of Claim 14: the condition number of the Vandermonde matrix A is plotted for $G = \mathrm{CH}_N$, $D = 2N-2$, and $1 \leq N \leq 64$. Left: $\mathrm{cond}\, A$ is bounded from above by 1.2. Right: $2^{1/4} - \mathrm{cond}\, A$ decays to zero (plot in log-scale).

Proof. Equivalently, we prove the injectivity of the linear map $f \in \mathcal{Y}_D^{\mathrm{ev}} \mapsto [f(\xi_i)]_{1 \leq i \leq M} \in \mathbb{R}^M$, where $\mathrm{CH}_N = \{\xi_i, 1 \leq i \leq M\}$. Assume that $f \in \mathcal{Y}_D^{\mathrm{ev}}$ is such that $f(\xi_i) = 0$, $\forall 1 \leq i \leq M$. We prove that $f = 0$. The key property is that f vanishes on every great circle $\mathscr{C}$ that contains at least $2D+1 = 4N-3$ zeros of f. Indeed, the restriction of $f \in \mathcal{Y}_D$ to $\mathscr{C}$, denoted by $f|_{\mathscr{C}}$, can be identified with a trigonometric polynomial with degree at most D. Such a trigonometric polynomial is null if it has at least $2D+1$ zeros. In the sequel, we especially apply this property to circles which permit to cover the sphere.

First, f vanishes on CS_N because the symmetry of f implies that $f(-\xi_i) = f(\xi_i) = 0$, for every $1 \leq i \leq M$. Second, the function f vanishes on the $2N$ meridian circles defined by

$$\mathscr{C}(\phi) = \{x(\theta, \phi),\, \theta \in [-\tfrac{\pi}{2}, \tfrac{\pi}{2}]\} \cup \{x(\theta, \phi+\pi),\, \theta \in [-\tfrac{\pi}{2}, \tfrac{\pi}{2}]\}, \quad \phi \equiv \tfrac{\pi}{4}\,(\tfrac{\pi}{2N}).$$

Indeed, for a given $\phi \equiv \frac{\pi}{4}\,(\frac{\pi}{2N})$, the assumption $N \leq 4$ implies that $\mathscr{C}(\phi)$ contains $4N$ points of CS_N. These points give $4N$ zeros for $f|_{\mathscr{C}(\phi)}$, so $f|_{\mathscr{C}(\phi)} = 0$. Third, the function f vanishes on every great circle $\mathscr{C}$ that does not contain the pole $(0,0,1)$, because such a circle contains $4N$ points on the set $\cup_{\phi \equiv \frac{\pi}{4}\,(\frac{\pi}{2N})} \mathscr{C}(\phi)$ and f vanishes on this set. □

Remark 16. In the proof, the key ingredient is that any meridian circle with longitude $\phi \equiv \frac{\pi}{4}\,(\frac{\pi}{2N})$ contains $4N$ points on CS_N if $N \leq 4$. For larger values of N, this property is not valid anymore.

Also, the following theorem proves that degrees larger than $2N-2$ must be proscribed in general; hence, the degree $D = 2N-2$ in Claim 14 is the largest "recommended" one.

Theorem 17. *For the grid $G = \mathrm{CH}_N$, and an even degree $D \geq 2N$, let A_N^D be the Vandermonde matrix* (6)*. Let $\sigma_{\min}(A_N^D)$, $\mathrm{cond}(A_N^D)$, denote its smallest singular value, resp. condition number.*

(i) For all $N \leq 4$ and $D \geq 2N$, the matrix A_N^D has not full column rank (hence, $\sigma_{\min}(A_N^D) = 0$, and $\mathrm{cond}(A_N^D) = +\infty$).

(ii) There exists a sequence $(\epsilon_N)_{N \geq 1}$ with asymptotics $\epsilon_N \underset{N \to +\infty}{\sim} \frac{N}{2}\left(\frac{2N}{\pi}\right)^{3/2}\left(\frac{2}{3}\right)^{2N} \underset{N \to +\infty}{\to} 0$, such that

$$\forall N \geq 1, \forall D \geq 2N, \quad \sigma_{\min}(A_N^D)^2 \leq \epsilon_N.$$

(iii) There is a sequence $(K_N)_{N \geq 1}$ with asymptotics $K_N \underset{N \to +\infty}{\sim} \frac{1}{4}\left(\frac{\pi}{2N}\right)^{1/2}\left(\frac{3}{2}\right)^{2N+1} \underset{N \to +\infty}{\to} +\infty$, such that, for all $N \geq 1$ and $D \geq 2N$ such that A_N^D has full column rank,

$$\mathrm{cond}(A_N^D)^2 \geq K_N.$$

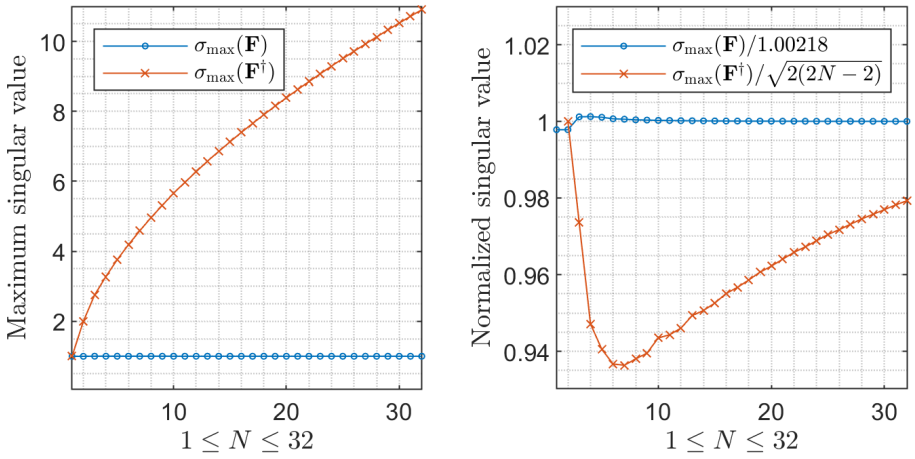

FIGURE 3. Stability constants associated to the discrete transforms F and $\mathrm{F}^\dagger$, in the case $G = \mathrm{CH}_N$, $D = 2N-2$. Left: the maximum singular values $\sigma_{\max}(\mathbf{F})$ and $\sigma_{\max}(\mathbf{F}^\dagger)$ are plotted in term of N. Right: the same singular values are plotted, but with "normalization" factors.

Proof. We refer to [7, Theorems 3–4], which establish similar results for the matrix

$$[Y_n^m(\xi)]_{\substack{\xi\in\mathrm{CS}_N \\ |m|\le n\le D}} \in \mathbb{R}^{(6N^2+2)\times(D+1)^2}.$$

The proofs are based on the examples $f_0 = Y_{2N}^{-2N}(x(\theta,\phi-\frac{\pi}{4})) \in \mathcal{Y}_{2N}$, $f_1 = Y_0 \in \mathcal{Y}_{2N}$. The same strategy applies for A_N^D, since f_0, $f_1 \in \mathcal{Y}_{2N}^{\mathrm{ev}}$, so we get almost the same estimations. The slight difference is a factor $\frac{1}{2}$ in (ii), due to the restriction of CS_N to CH_N. This factor disappears in the estimation of the condition number in (iii), since it is a ratio.

To put it in a nutshell, the function f_0 is the key of the proof. There is some trigonometric polynomial p such that

$$f_0(x(\theta,\phi)) = p(\theta)\sin(2N(\phi-\tfrac{\pi}{4})), \quad \theta\in[-\tfrac{\pi}{2},\tfrac{\pi}{2}],\ \phi\in\mathbb{R},$$

where $p(\theta)$ becomes small when θ moves away from 0. Therefore, f_0 vanishes on CS_N intersected with the meridian circles $\phi \equiv \frac{\pi}{4}\,(\frac{\pi}{2N})$. Hence, if $N \le 4$, f_0 vanishes on CH_N, which implies (i). Otherwise, the remaining non-zero values of $f_0|_{\mathrm{CH}_N}$ are bounded from above considering some estimation of p. We refer to the proof of [7, Theorems 3–4] for additional details. □

Remark 18. The critical degree $2N$ corresponds usually to oscillations at the Nyquist's frequency for a uniform one-dimensional grid with step $\frac{\pi}{2N}$. Here, our critical example f_0 oscillates at this frequency along the (equatorial) grid $\phi \equiv \frac{\pi}{4}\,(\frac{\pi}{2N})$, so that f_0 is undersampled along the equator.

In the sequel, if the grid is $G = \mathrm{CH}_N$, then we select the degree $D = 2N-2$, as a consequence of Claim 14 and Theorem 17.

4.3. **Discrete Funk transform.** Assuming that Claim 14 is true, we consider the discrete Funk transform F, in the case $G = \mathrm{CH}_N$, $D = 2N-2$, where $N \ge 1$ is fixed. Of course, any result of Subsection 3.2 applies. In particular, Theorem 11 guarantees estimations of stability based on the condition number plotted in Figure 2. We check this point in Figure 3, where we observe that the maximum singular values satisfy

$$\sigma_{\max}(\mathbf{F}) \approx 1.00218, \quad \sigma_{\max}(\mathbf{F}^\dagger) \approx \sqrt{2(2N-2)}, \qquad 1 \le N \le 32;$$

this is in agreement with the theoretical bounds (18).

5. Numerical results

We perform various numerical experiments, in order to assess the quality and the efficiency of the discrete Funk transform on the Cubed Hemisphere.

5.1. **Accuracy and convergence of the discrete Funk transform.** We evaluate the accuracy of the discrete Funk transform when it is used to approximate Funk transforms from values on CH_N.

For that purpose, we introduce test functions,

$$g^{(k)} := \sum_{\substack{0\leq n\leq 100\\ n\equiv 0\,(2)}} \sum_{-n\leq m\leq n} \hat{g}_n^{(k)}(2+0.5\cos(m)+0.25\sin(m))\,Y_n^m \in \mathcal{Y}_{100}^{\mathrm{ev}}, \tag{20}$$

$$\hat{g}_n^{(-\infty)} := \tfrac{1}{n!}, \quad \hat{g}_n^{(k)} := (n+1)^k,\ k=-6,\,-4,\,-2,\,-1,\,0, \tag{21}$$

where the various rates of decay of the spectral coefficients encode various "smoothness" properties. Here, $g^{(k)} \in \mathcal{Y}_{100}^{\mathrm{ev}}$, so we compute the Funk transform $\mathcal{F}g^{(k)}$ by Theorem 6, with $G=\mathrm{CH}_N$, $N=51$ and $D=2N-2$. For any $\alpha\in\mathbb{S}^2$, we use the relation (12) to compute $\mathcal{F}g^{(k)}(\alpha)$ from the values of $g^{(k)}$ on the grid CH_{51}. This computation is exact, up to rounding errors.

Consider now the discrete Funk transform F, associated to the grid $G=\mathrm{CH}_N=\{\xi_i, 1\leq i\leq M\}$ and the degree $D=2N-2$. For any function g, we approximate the vector $[(\mathcal{F}g)(\xi_i)]_{1\leq i\leq M}$ by $\mathbf{F}[g(\xi_i)]_{1\leq i\leq M}$ with a relative error $\eta_N[g]$ defined by

$$\eta_N[g] := \frac{\|\mathbf{F}[g(\xi_i)]_{1\leq i\leq M} - [(\mathcal{F}g)(\xi_i)]_{1\leq i\leq M}\|}{\|[(\mathcal{F}g)(\xi_i)]_{1\leq i\leq M}\|}; \tag{22}$$

here, $\|\cdot\|$ denotes the euclidean norm in $\mathbb{R}^M$. For $g=g^{(k)}$, the reference vector $[(\mathcal{F}g^{(k)})(\xi_i)]_{1\leq i\leq M}$ is computed as mentioned in the previous paragraph (relation (12) with CH_{51} for the data grid, and $\alpha\in\mathrm{CH}_N$ for the evaluation). In particular, $\eta_{51}[g^{(k)}]$ is zero (up to rounding errors).

We have plotted the errors $\eta_N[g^{(k)}]$ in Figure 4 (left panel), for $1\leq N\leq 32$. Overall, the behavior of the observed error depends on the rate of decay of the spectral coefficients; the error converges fastly to zero for rapidly decaying coefficients. We quantify this phenomenon in Table 1, where we report numerical convergence rates $r_N[g]$ such that

$$\eta_{2N}[g] = \eta_N[g]\,2^{-r_N[g]}, \quad \text{with} \quad r_N[g] = \log_2\eta_N[g] - \log_2\eta_{2N}[g]. \tag{23}$$

N	$r_N[g^{(-\infty)}]$	$r_N[g^{(-6)}]$	$r_N[g^{(-4)}]$	$r_N[g^{(-2)}]$	$r_N[g^{(-1)}]$	$r_N[g^{(0)}]$
1	3.7	4.5	2.9	0.28	-1.4	1.8
2	11	4.9	3.1	1.3	0.3	-0.19
4	29	5.4	3.4	1.5	0.78	-0.11
8	5.3	5.4	3.4	1.8	1.2	0.093
16	0.83	5.5	3.6	2.2	1.8	1

Table 1. Convergence rates (23) of the errors (22), for the test functions from (20-21).

For $g^{(-\infty)}$, with a factorial decay of the coefficients, $\hat{g}_n^{(-\infty)} = 1/n!$, the very fast convergence appears as a blow up of the rate $r_N[g^{(-\infty)}]$. For the functions $g^{(-k)}$, $k=6,\,4,\,2$, with a decay $\hat{g}_n^{(-k)} = 1/(n+1)^k$, the rate looks like $r_N[g^{(-k)}] \approx k-0.5$. For $g^{(-1)}$, with the slow decay $\hat{g}_n^{(-1)} = 1/(n+1)$, and $g^{(0)}$ with constant values $\hat{g}_n^{(0)} = 1$, the convergence analysis is not so clear.

In a word, the discrete Funk transform F (or its matrix $\mathbf{F}$) approximates the Funk transform from values on a Cubed Hemisphere. It converges fastly for smooth functions, for which the spectral coefficients decay rapidly to zero. The observed rates of convergence suggests to analyze theoretically the speed of convergence in Sobolev spaces. We defer this point to further studies.

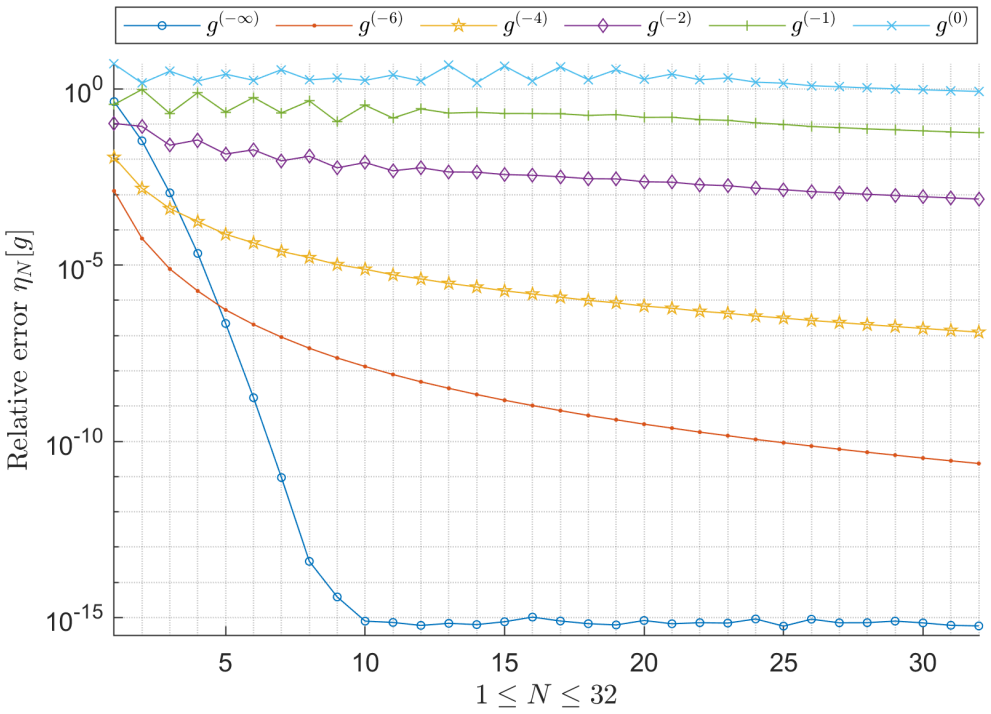

FIGURE 4. Approximation of the Funk transform $[(\mathcal{F}g)(\xi_i)]_{1\leq i\leq M}$ by the discrete transform $\mathbf{F}[g(\xi_i)]_{1\leq i\leq M}$, for the grid CH_N, and the degree $2N-2$. The relative error $\eta_N[g]$ in (22) is plotted, for each test function $g = g^{(k)}$ from (20-21).

5.2. **Funk transform of Gaussian models.** We study the accuracy of the discrete Funk transform on Gaussian models from dMRI, for the grid $G = \mathrm{CH}_N$ and the degree $D = 2N-2$.

We consider Gaussian models in the following form,

$$S(x) = \exp(-b\, x^{\intercal}\mathbf{D}x), \quad x \in \mathbb{S}^2, \tag{24}$$

where $b \geq 0$, and $\mathbf{D} \in \mathbb{R}^{3\times 3}$ is a symmetric positive definite matrix. Such models describe the dMRI signal S in Diffusion Tensor Imaging. The so-called *diffusion tensor* $\mathbf{D}$ models intrinsic diffusion properties of biological tissues. The parameter b is the so-called *b-value*, and is a parameter of the acquisition. The unit vector x, represents a *gradient direction*, and browses a hemispherical grid during the acquisition. Gaussian models such as (24) appear also in High Angular Resolution Diffusion Imaging [11]. In this field, a weighted average of several Gaussian models can be introduced to model the signal from crossing fibers. The orientation of the fibers can be imaged using an Orientation Distribution Function, which is computed approximately as the Funk transform of the recorded signal S [12, 41]. Hence, it is crucial to be able to compute accurately the Funk transform of a Gaussian model, from a discrete set of values.

In this paper, we consider Gaussian signals

$$S_j(x) = \exp(-b_j\, x^{\intercal}\mathbf{D}_j x), \quad x \in \mathbb{S}^2, \quad 1 \leq j \leq 6. \tag{25}$$

The b-values b_j and the diffusion tensors $\mathbf{D}_j$ are defined in Table 2. Our values are inspired by the values from [12]. The b-value $b = 1000$ [s/mm^2] is an usual clinical value, whereas $b = 3000$ [s/mm^2] is considered as relatively high. For the diffusion tensors, we have chosen diagonal matrices $\mathbf{D}_i$, defined by the eigenvalues μ_1, μ_2, $\mu_3 > 0$. The matrix $\mathbf{D}_3$ has been found in the synthetic data generation in [12]. The other matrices have been defined as "variations" of this matrix, in order to obtain more or less anisotropy; see the last column of Table 2, where anisotropy is measured by means of the *fractional anisotropy* (FA),

$$\mathrm{FA} = \frac{1}{\sqrt{2}}\sqrt{\frac{(\mu_1-\mu_2)^2+(\mu_1-\mu_3)^2+(\mu_2-\mu_3)^2}{\mu_1^2+\mu_2^2+\mu_3^2}} \in [0,1]. \tag{26}$$

j	b_j [s/mm^2]	$\mathbf{D}_j$ [mm^2/s]	FA
1	1000	$10^{-6}\,\mathrm{diag}(300, 300, 300)$	0
2	1000	$10^{-6}\,\mathrm{diag}(300, 600, 900)$	0.46
3	1000	$10^{-6}\,\mathrm{diag}(300, 300, 1700)$	0.80
4	3000	$10^{-6}\,\mathrm{diag}(300, 300, 300)$	0
5	3000	$10^{-6}\,\mathrm{diag}(300, 600, 900)$	0.46
6	3000	$10^{-6}\,\mathrm{diag}(300, 300, 1700)$	0.80

TABLE 2. Parameters of the Gaussian signals (25). The anisotropy is measured by the fractional anisotropy (FA), defined in (26).

Firstly, we assume that the (even) signal S_j is recorded on $G = \mathrm{CH}_N$, with $N \geq 1$ and $1 \leq j \leq 6$. We compute reference values $[(\mathcal{F}S_j)(\xi_i)]_{1\leq i\leq M}$ using trapezoidal rules[3]. Then, we compute the discrete Funk transform $\mathbf{F}[S_j(\xi_i)]_{1\leq i\leq M}$. It approximates $[(\mathcal{F}S_j)(\xi_i)]_{1\leq i\leq M}$, with a relative error $\eta_N[S_j]$, where η_N is defined in (22). We have plotted these errors in Figure 5 (left panel) to evaluate the accuracy of the procedure. Overall, a fast convergence due to the smoothness of the Gaussian signals is observed. For the isotropic functions S_1 and S_4, the error is always zero (up to rounding errors), because S_1, $S_4 \in \mathcal{Y}_0 \subset \mathcal{Y}^{\mathrm{ev}}_{2N-2}$, so (11) applies. With S_2, S_5, and S_3, S_6, we observe that increasing the b-value induces a loss in accuracy; this is because a Gaussian becomes sharper with high b-values.

Secondly, we show that the orientation of the grid does not matter. For that purpose, we consider "rotations" of the signals S_j:

$$S_j(Q^\intercal \cdot) : x \mapsto S_j(Q^\intercal x) = \exp(-b\, x^\intercal\, Q\mathbf{D}_j Q^\intercal\, x),$$

where $Q \in \mathbb{R}^{3\times 3}$ is a random orthogonal matrix. The relative error of approximation of the Funk transform becomes $\eta_N[S_j(Q^\intercal\cdot)]$, and can be computed as before. For each function S_j, we repeat this procedure for 30 random orthogonal matrices Q, and we plot the maximum error

$$\max_Q \eta_N[S_j(Q^\intercal\cdot)] \tag{27}$$

in Figure 5 (right panel). We obtain a similar conclusion than before, so that the conclusion does not depend on the orientation of the grid.

Thirdly, we investigate the effect of noise. We corrupt the signals as follows. We fix a value of N. For any $1 \leq j \leq 6$, for any $\sigma = 2^{-p}$, with $2 \leq p \leq 31$, we corrupt S_j, by a "speckle" noise and an additive noise with level σ:

$$S_j^\sigma(\xi_i) = |S_j(\xi_i)(1 + \sigma u_i) + \sigma v_i|, \quad 1 \leq i \leq M,$$

where the u_i, v_i, are $2M = 6N^2 + 2$ independent realizations of the normal law $\mathcal{N}(0, 1)$. In this case, the relative error on the signal is given by

$$\frac{\|[S_j^\sigma(\xi_i) - S_j(\xi_i)]_{1\leq i\leq M}\|}{\|[S_j(\xi_i)]_{1\leq i\leq M}\|}. \tag{28}$$

We compute the discrete Funk transform $\mathbf{F}[S_j^\sigma(\xi_i)]_{1\leq i\leq M}$, which approximates $[(\mathcal{F}S_j)(\xi_i)]_{1\leq i\leq M}$ with a relative error

$$\frac{\|\mathbf{F}[S_j^\sigma(\xi_i)]_{1\leq i\leq M} - [(\mathcal{F}S_j)(\xi_i)]_{1\leq i\leq M}\|}{\|[(\mathcal{F}S_j)(\xi_i)]_{1\leq i\leq M}\|}. \tag{29}$$

In Figure 6, we have plotted the relative error (29) on the transform against the relative error (28) on the signal. Two values of N are considered. On the left, $N = 5$, so that the grid CH_N contains 76 points, and the approximation space is $\mathcal{Y}^{\mathrm{ev}}_8$. On the right, $N = 10$, so that the grid CH_N contains 301 points, and the approximation space is $\mathcal{Y}^{\mathrm{ev}}_{18}$. Roughly speaking, we observe that the

[3]Here, an integral along a great circle $x \cdot \alpha = 0$ is an integral of a smooth 2π-periodic function over a period, so the trapezoidal rule converges exponentially to the true integral [40]. Therefore, we apply successive trapezoidal rules as follows. We start with an angular step $\frac{\pi}{8}$. We evaluate the associated trapezoidal rule; then, we divide the angular step by two, and we iterate. The iterations are stopped as soon as the relative increase of the value between two successive iterations is below the tolerance 10^{-13}.

relative error on the transform is the maximum between the relative error on the signal, and the relative error on the transform from the noise-free case (displayed in Figure 5). This result is in agreement with the stability constant of the transform $\mathbf{F}$, $\sigma_{\max}(\mathbf{F}) \approx 1$ in Figure 3.

To conclude, the Funk transform of Gaussian models can be accurately evaluated by the discrete transform on the Cubed Hemisphere, and in a very stable way.

5.3. **Comparison of the Cubed Sphere and the icosahedral grid.** We compare discrete Funk transforms on Cubed Hemispheres with discrete Funk transforms on icosahedral grids.

For the Cubed Sphere, we consider the Cubed Hemisphere CH_N with cardinal number $M = 3N^2 + 1$. As an alternative grid, we consider an *icosahedral grid*. It is based on a regular triangular lattice onto each face of an icosahedron inscribed in $\mathbb{S}^2$. The icosahedral grid is defined as the projection of the vertices of this lattice onto $\mathbb{S}^2$. We further halve the grid by symmetry consideration (Proposition 2), in the same way as CS_N has been halved. Assuming that each edge of the original icosahedron has been divided into N parts, the resulting half-grid contains $M = 5N^2 + 1$ points; we still call this grid an *icosahedral grid*, and we denote it by Ico_N. Such grids have already been used for computing Funk transforms in [12] with $M = 81, 321$ (which corresponds to the parameters $N = 2, 8$).

Firstly, in order to obtain a stable discrete Funk transform, the degree D must be carefully tuned. For CH_N, we use the rule $D = 2N - 2$, as it has been introduced in Section 4. For the icosahedral grid Ico_N, we do not know such a rule on the degree. To overcome this disadvantage, we compute numerically D as the largest degree D such that $\operatorname{cond} A \leq 2$, where A denotes the Vandermonde matrix (6) with $G = \mathrm{Ico}_N$. In Figure 7, we plot the obtained degree D against the number of points of the grid, for the grid CH_N with $1 \leq N \leq 32$, and the grid Ico_N with $1 \leq N \leq 25$. We observe that for equivalent number of grid points, the degree associated to the icosahedral grid is larger than the degree associated to the Cubed Hemisphere. Therefore, the icosahedral grid permits to work in a larger approximation space $\mathcal{Y}_D^{\mathrm{ev}}$, while keeping a very small condition number ($\operatorname{cond} A \leq 2$).

Secondly, we consider successively the discrete Funk transform associated to the grids

$$G = \mathrm{CH}_N,\ 1 \leq N \leq 32, \quad G = \mathrm{Ico}_N,\ 1 \leq N \leq 25,$$

with the degree D discussed above. We evaluate the accuracy on the test function $g = g^{(k)}$ defined in (20-21), for $k = -\infty, -6, -4, -2$, by means of the relative error

$$\eta[g] = \max_Q \frac{\|\mathbf{F}[g(Q^\intercal \xi_i)]_{1\leq i\leq M} - [(\mathcal{F}g)(Q^\intercal \xi_i)]_{1\leq i\leq M}\|}{\|[(\mathcal{F}g)(Q^\intercal \xi_i)]_{1\leq i\leq M}\|}, \quad (G = \{\xi_i, 1 \leq i \leq M\}); \tag{30}$$

here the "orientation" Q browses a set of 30 random orthogonal matrices. The computed errors are displayed in Figure 8. Overall, the two grids define transforms with similar accuracy, and similar properties of convergence. This test reveals also that for very smooth functions and very small grids, the isosahedral grid defines a more accurate transform.

Lastly, we repeat the same procedure, but we corrupt the data with a level of noise $\sigma = 10^{-6}$. We compute the relative error

$$\eta_{\mathrm{noise}}[g] = \max_{(Q,u,v)} \frac{\|\mathbf{F}[g(Q^\intercal \xi_i)(1 + \sigma u_i) + \sigma v_i]_{1\leq i\leq M} - [(\mathcal{F}g)(Q^\intercal \xi_i)]_{1\leq i\leq M}\|}{\|[(\mathcal{F}g)(Q^\intercal \xi_i)]_{1\leq i\leq M}\|}, \quad \sigma = 10^{-6}, \tag{31}$$

where the maximum is taken over 30 experiments; each experiment fixes Q as a random orthogonal matrix, and the u_i, v_i as $2M$ independent realizations of the normal law $\mathcal{N}(0, 1)$. The obtained errors are depicted in Figure 9. The observations of the noise-free case still apply. We further observe that the errors are almost the same as soon as the noise becomes dominant.

To conclude, considering the Cubed Sphere is simpler than considering an icosahedral grid, for which further studies (or computation) are needed to keep the conditioning under control. Moreover, the resulting accuracy is almost the same, except for very smooth functions on very small grids; in this case, the icosahedral grid is more advantageous if the noise is small enough.

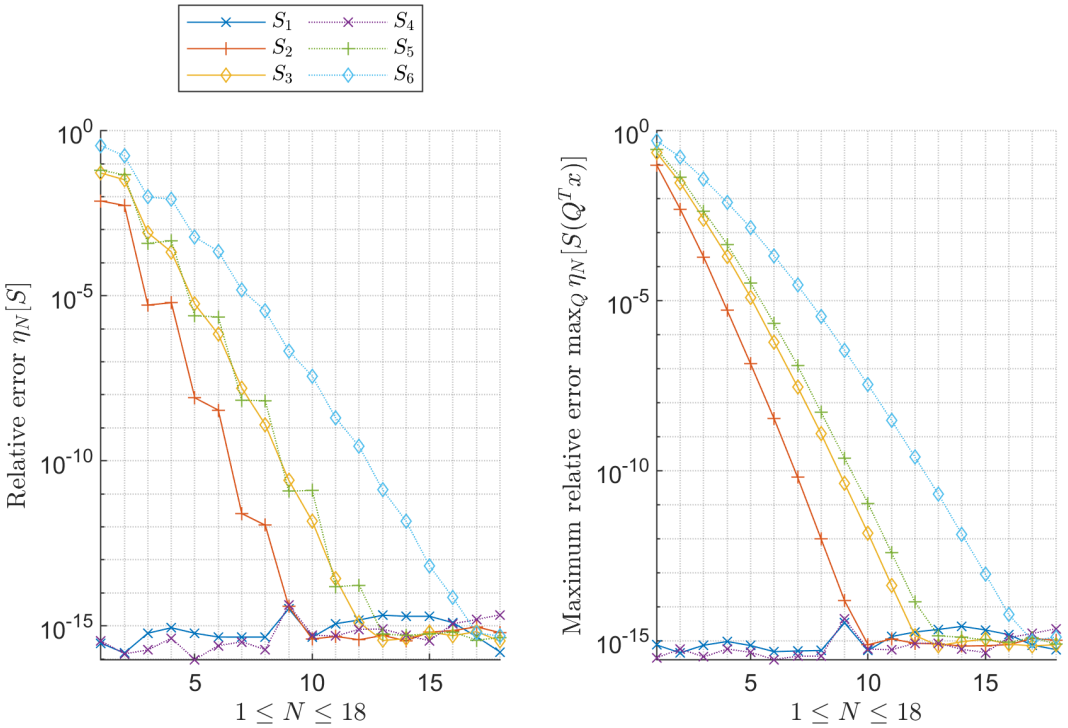

FIGURE 5. Accuracy of the discrete Funk transform on CH_N with degree $2N-2$, for the Gaussian signals S_j in (25) and Table 5. Left: $\mathbf{F}[S_j(\xi_i)]_{1\leq i\leq M}$ approximates $[(\mathcal{F}S_j)(\xi_i)]_{1\leq i\leq M}$ with relative error $\eta_N[S_j]$ in (22); we plot $\eta_N[S_j]$ with $1 \leq N \leq 32$. Right: for any orthogonal matrix $Q \in \mathbb{R}^{3\times 3}$, the same procedure applied to the "rotated" Gaussian $S_j(Q^\intercal \cdot)$ results in a relative error $\eta_N[S_j(Q^\intercal \cdot)]$; we plot the maximum error (27), where Q scans a set of 30 random orthogonal matrices.

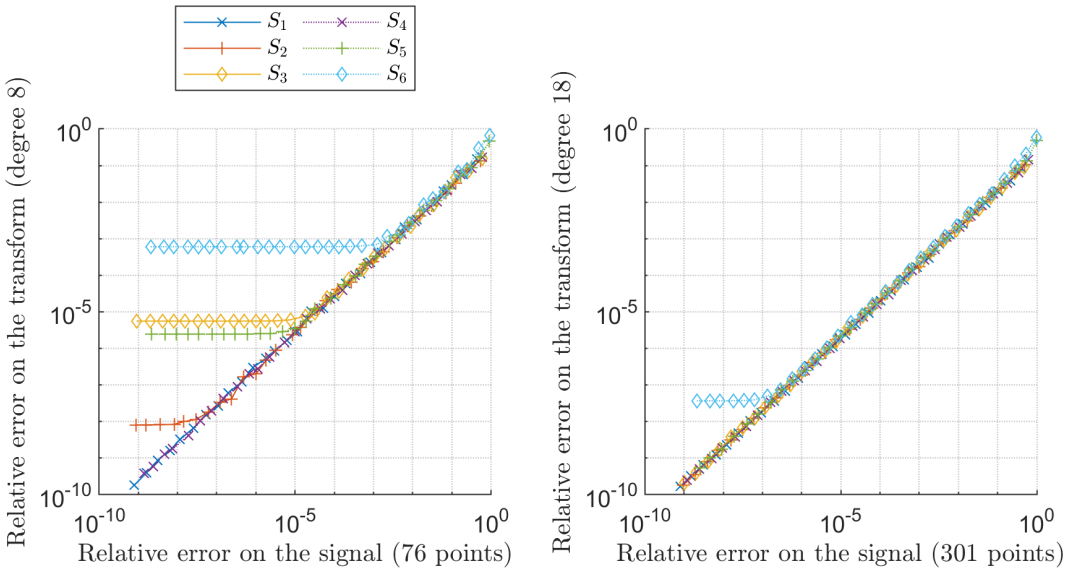

FIGURE 6. Accuracy of the discrete Funk transform on CH_N (degree $2N-2$), for Gaussian signals S_j corrupted by noise. The relative error (29) on the transform is plotted against the relative error (29) on the signal (logarithmic scale). Left: $N = 5$; right: $N = 10$.

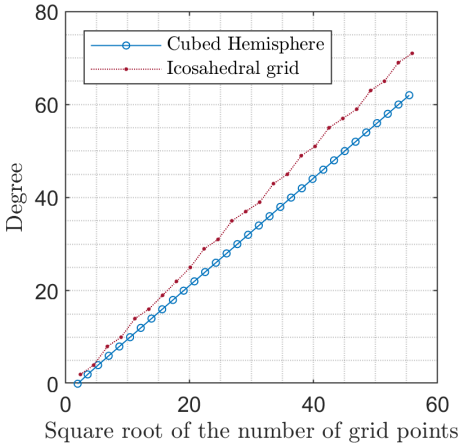

FIGURE 7. Degree D for least squares fitting on the Cubed Hemisphere CH_N, resp. the Icosahedral grid Ico_N. For CH_N, the number of grid points is $M = 3N^2 + 1$, the degree is $D = 2N - 2$, and $1 \leq N \leq 32$. For Ico_N, $M = 5N^2 + 1$, D is the largest degree such that $\operatorname{cond} A \leq 2$, and $1 \leq N \leq 25$.

5.4. **Computation time.** As a further indicator of efficiency, we measure the computation time of discrete Funk transforms, for the grid $G = \mathrm{CH}_N$, and the degree $D = 2N - 2$. For each value of N, we fix a random vector $\boldsymbol{b}$, and we measure the time dedicated to the assembly of the matrix A and the computation of $\mathbf{F}\boldsymbol{b}$. The code is written in Matlab, and $\ell[b]$ is computed with a simple command such as `(A'*A)\(A'*b)`. The program is executed on a laptop Dell Precision 7540; the processor is an Intel i9-9880H@2.30 GHz. The experiment is repeated six times, and we report the average values of the running times in Table 3.

Parameter N	1	2	4	8	16	32	64
Number of grid points M	4	13	49	193	769	3073	12289
Degree D	0	2	6	14	30	62	126
CPU time (s)	1.8e-04	1.2e-04	3.7e-04	2.3e-03	2.2e-02	5.0e-01	1.5e+01

TABLE 3. Running time dedicated to the computation of a discrete Funk transform $\mathbf{F}\boldsymbol{b}$, for the grid $G = \mathrm{CH}_N$, and the degree $D = 2N - 2$.

These preliminary results show that our transform is computed relatively fastly for small grids, despite our "brute force" implementation has not been optimized. Further studies are required to decrease these times. Combining symmetry consideration and an iterative solver such as Conjugate Gradient Least Squares (CGLS) is an option to consider in the future.

6. CONCLUSION

This paper deals with mathematical and numerical properties of some discrete Funk transforms, including their (pseudo)inversion. As a special case, the study includes a simple framework based on the Cubed Sphere. Our theoretical and numerical results indicate that stability and suitable convergence properties are expected in this context, despite regularization has not been applied. This mathematical background about discrete Funk transforms could potentially have applications in any field where integrals along great circles on a sphere are considered.

This work opens problems to be addressed in the future. Finding the "best" spherical grid and the "best" degree is an open question. For the case of the Cubed Hemisphere CH_N, proving that our rule on the degree ($D = 2N - 2$) results in a small condition number is still open. Another point concerns the speed of convergence, which should be quantified, for instance in Sobolev spaces. Concerning implementation aspects, writing a "fast" algorithm has still to be done. A first step in this direction could be an efficient solver for the least squares problem,

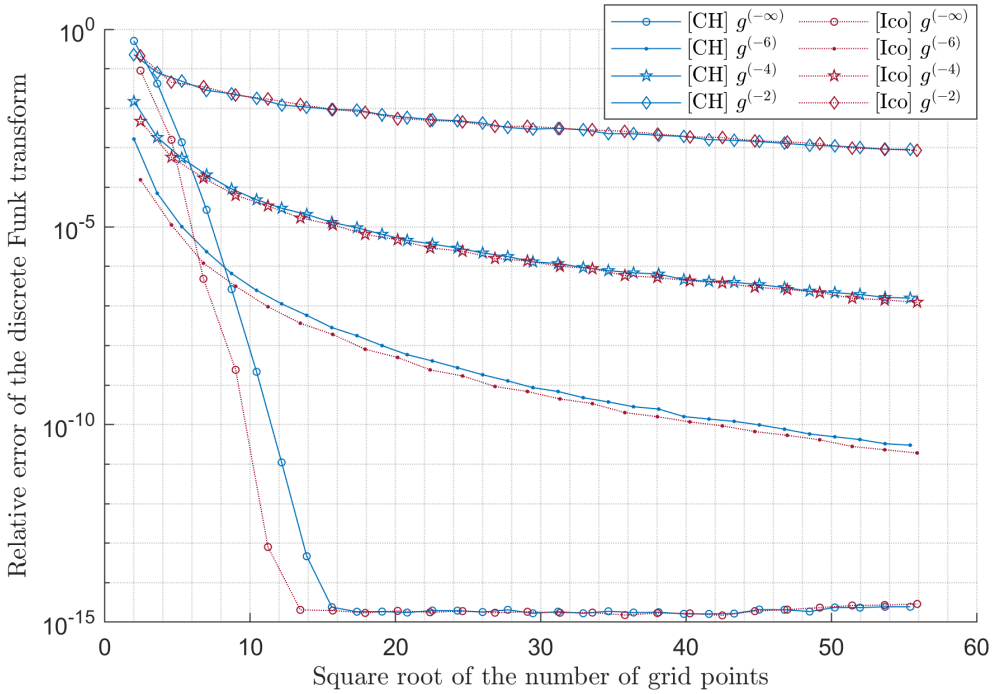

FIGURE 8. Accuracy of the Funk transform associated to the Cubed Hemisphere (CH), resp. the Icosahedral grid (Ico). The relative error $\eta[g]$ in (30) is plotted against $\sqrt{M}$, with M the number of grid points. The degree D is plotted in Figure 7.

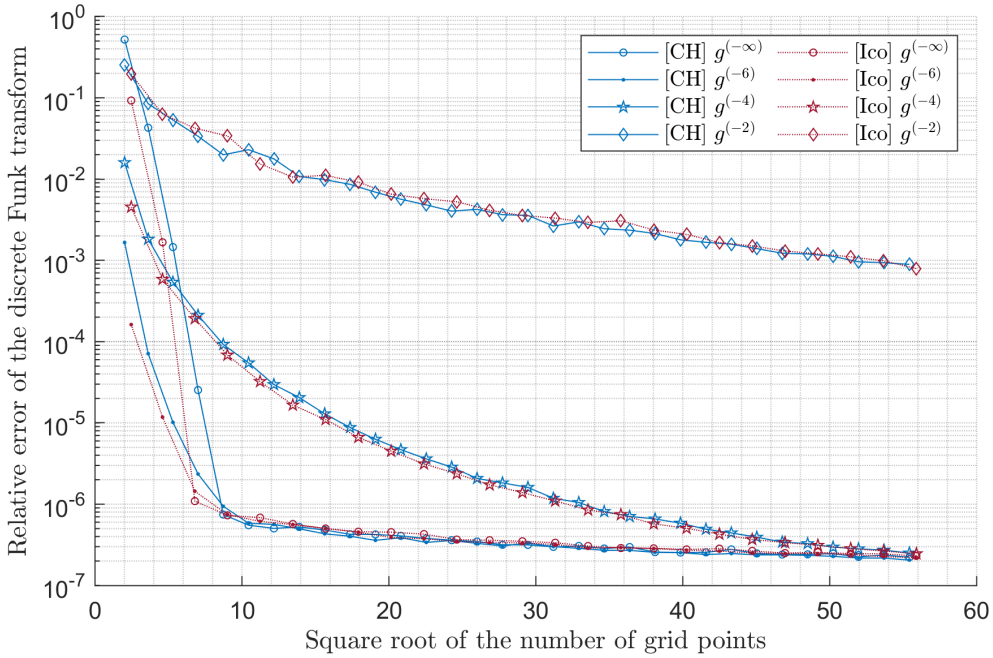

FIGURE 9. Accuracy of the Funk transform associated to the Cubed Hemisphere (CH), resp. the Icosahedral grid (Ico), with a level of noise $\sigma = 10^{-6}$. The relative error $\eta_{\text{noise}}[g]$ in (31) is plotted against $\sqrt{M}$, with M the number of grid points. The degree D is plotted in Figure 7.

taking into account further symmetry consideration. To finish with, comparing our transform with time-tested transforms on real experiments is a goal for further studies; in particular, testing the Cubed Hemisphere in Q-ball imaging may be instructive.

Acknowledgments

The author wishes to express his thanks to the anonymous referee for the many helpful suggestions on how to improve the manuscript.

References

[1] A. C. Aitken. *Determinants and matrices*. New York: interscience publishers, third edition, 1944.

[2] C. An, X. Chen, I. H. Sloan, and R. S. Womersley. Well Conditioned Spherical Designs for Integration and Interpolation on the Two-Sphere. *SIAM journal on numerical analysis*, 48(6):2135–2157, 2010.

[3] C. An, X. Chen, I. H. Sloan, and R. S. Womersley. Regularized least squares approximations on the sphere using spherical designs. *SIAM Journal on numerical analysis*, 50(3):1513–1534, 2012.

[4] J.-B. Bellet. Symmetry group of the equiangular cubed sphere. *Quarterly of Applied Mathematics*, 80:69–86, 2022.

[5] J.-B. Bellet, M. Brachet, and J.-P. Croisille. Quadrature and symmetry on the Cubed Sphere. *Journal of Computational and Applied Mathematics*, 409, 2022.

[6] J.-B. Bellet, M. Brachet, and J.-P. Croisille. Interpolation on the Cubed Sphere with Spherical Harmonics. *Numerische Mathematik*, to appear.

[7] J.-B. Bellet and J.-P. Croisille. Least Squares Spherical Harmonics Approximation on the Cubed Sphere. *https://hal.archives-ouvertes.fr/hal-03788836*, 2022. Under revision.

[8] M. Brachet. *Schémas compacts hermitiens sur la Sphère: applications en climatologie et océanographie numérique*. PhD thesis, Université de Lorraine, 2018 (in French).

[9] X. Chen, R. S. Womersley, and J. J. Ye. Minimizing the condition number of a Gram matrix. *SIAM Journal on optimization*, 21(1):127–148, 2011.

[10] S. Chevrot, R. Martin, and D. Komatitsch. Optimized discrete wavelet transforms in the cubed sphere with the lifting scheme—implications for global finite-frequency tomography. *Geophysical Journal International*, 191(3):1391–1402, 2012.

[11] M. Descoteaux. *High Angular Resolution Diffusion Imaging (HARDI)*, pages 1–25. John Wiley & Sons, Ltd, 2015.

[12] M. Descoteaux, E. Angelino, S. Fitzgibbons, and R. Deriche. Regularized, Fast, and Robust Analytical Q-Ball Imaging. *Magnetic Resonance in Medicine*, 58:497–510, 2007.

[13] P. Funk. Über Flächen mit lauter geschlossenen geodätischen Linien. *Mathematische Annalen*, 1913.

[14] G. H. Golub and C. F. Van Loan. *Matrix computations*. The Johns Hopkins University Press, third edition, 1996.

[15] P. C. Hansen. *Rank-deficient and discrete ill-posed problems: numerical aspects of linear inversion*, volume 4. Siam, 2005.

[16] D. P. Hardin, T. Michaels, and E. B. Saff. A Comparison of Popular Point Configurations on S^2. *Dolomites Research Notes on Approximation*, 9(1):16–49, 2016.

[17] C. P. Hess, P. Mukherjee, E. T. Han, D. Xu, and D. B. Vigneron. Q-Ball Reconstruction of Multimodal Fiber Orientations Using The Spherical Harmonic Basis. *Magnetic Resonance in Medicine*, 56(1):104–117, 2006.

[18] K. Hesse, I. H. Sloan, and R. S. Womersley. Numerical integration on the sphere. In W. Freeden, Z. M. Nashed, and T. Sonar, editors, *Handbook of Geomathematics*. Springer, 2010.

[19] R. Hielscher and M. Quellmalz. Reconstructing a function on the sphere from its means along vertical slices. *Inverse Problems and Imaging*, 10(3):711–739, 2016.

[20] Y. Hristova, S. Moon, and D. Steinhauer. A radon-type transform arising in photoacoustic tomography with circular detectors: spherical geometry. *Inverse Problems in Science and Engineering*, 24(6):974–989, 2016.

[21] L. Ivan, H. De Sterck, S. A. Northrup, and C. P. T. Groth. Multi-dimensional finite-volume scheme for hyperbolic conservation laws on three-dimensional solution-adaptive cubed-sphere grids. *Journal of Computational Physics*, 255:205–227, 2013.

[22] J. H. Jensen, G. R. Glenn, and J. A. Helpern. Fiber Ball Imaging. *NeuroImage*, 124:824–833, 2016.

[23] B. A. Jones, G. H. Born, and G. Beylkin. Comparison of the Cubed-Sphere Gravity Model with the Spherical Harmonics. *Journal of Guidance, Control, and Dynamics*, 33(2):415–425, 2010.

[24] H.-G. Kang and H.-B. Cheong. An efficient implementation of a high-order filter for a cubed-sphere spectral element model. *Journal of Computational Physics*, 332:66–82, 2017.

[25] S. Kazantsev. Funk–Minkowski transform and spherical convolution of Hilbert type in reconstructing functions on the sphere. *Siberian Electronic Mathematical Reports*, 15:1630–1650, 2018.

[26] S. Kunis. A note on stability results for scattered data interpolation on euclidean spheres. *Advances in Computational Mathematics*, 30:303–314, 2009.

[27] S. Kunis, H. M. Möller, and U. von der Ohe. Prony's method on the sphere. *The SMAI Journal of Computational Mathematics*, 5:87–97, 2019.

[28] D. Lee and A. Palha. A mixed mimetic spectral element model of the rotating shallow water equations on the cubed sphere. *Journal of Computational Physics*, 375:240–262, 2018.
[29] A. K. Louis, M. Riplinger, M. Spiess, and E. Spodarev. Inversion algorithms for the spherical radon and cosine transform. *Inverse Problems*, 27(3):035015, 2011.
[30] J. L. McGregor. Semi-Lagrangian Advection on Conformal-Cubic Grids. *Monthly Weather Review*, 124(6):1311–1322, 1996.
[31] R. D. Nair, S. J. Thomas, and R. D. Loft. A Discontinuous Galerkin Transport Scheme on the Cubed Sphere. *Monthly Weather Review*, 133(4):814–828, 2005.
[32] R. J. Purser and M. Rančić. Smooth quasi-homogeneous gridding of the sphere. *Quarterly Journal of the Royal Meteorological Society*, 124(546):637–647, 1998.
[33] W. M. Putman. *Development of the finite-volume dynamical core on the cubed-sphere*. PhD thesis, The Florida State University, 2007.
[34] M. Quellmalz. A generalization of the Funk–Radon transform. *Inverse Problems*, 33(3):035016, 2017.
[35] M. Rančić, R. J. Purser, and F. Mesinger. A global shallow-water model using an expanded spherical cube: Gnomonic versus conformal coordinates. *Quarterly Journal of the Royal Meteorological Society*, 122(532):959–982, 1996.
[36] C. Ronchi, R. Iacono, and P. S. Paolucci. The "cubed sphere": a new method for the solution of partial differential equations in spherical geometry. *Journal of Computational Physics*, 124(1):93–114, 1996.
[37] B. Rubin. Inversion formulas for the spherical Radon transform and the generalized cosine transform. *Advances in Applied Mathematics*, 29(3):471–497, 2002.
[38] R. Sadourny. Conservative finite-difference approximations of the primitive equations on quasi-uniform spherical grids. *Monthly Weather Review*, 100(2):136–144, 1972.
[39] S. J. Thomas, J. M. Dennis, H. M. Tufo, and P. F. Fischer. A Schwarz preconditioner for the cubed-sphere. *SIAM Journal on Scientific Computing*, 25(2):442–453, 2003.
[40] L. N. Trefethen and J. A. C. Weideman. The Exponentially Convergent Trapezoidal Rule. *SIAM Review*, 56(3):385–458, 2014.
[41] D. S. Tuch. Q-Ball Imaging. *Magnetic Resonance in Medicine*, 52:1358–1372, 2004.
[42] D. L. Williamson. The evolution of dynamical cores for global atmospheric models. *Journal of the Meteorological Society of Japan. Ser. II*, 85B:241–269, 2007.
[43] C. E. Yarman and B. Yazici. Inversion of Circular Averages using the Funk Transform. In *2007 IEEE International Conference on Acoustics, Speech and Signal Processing - ICASSP '07*, volume 1, pages I–541–I–544, 2007.
[44] G. Zangerl and O. Scherzer. Exact reconstruction in photoacoustic tomography with circular integrating detectors II: Spherical geometry. *Mathematical Methods in the Applied Sciences*, 33(15):1771–1782, 2010.

Université de Lorraine, CNRS, IECL, F-57000 Metz, France
Email address: jean-baptiste.bellet@univ-lorraine.fr